Journal of Visualization, Vol. 3, No. 2 (2000) 101-113

3-D PTV Measurement on Turbulence Modification Due to an Oil Droplet in a Plane Couette Water Flow

Hagiwara, Y.*1, Nishino, M.*2, Tanaka, M.*1 and Sakamoto, S.*3

*1 Department of Mechanical and System Engineering, Kyoto Institute of Technology, Matsugasaki, Sakyo-ku, Kyoto 606-8585, Japan.
*2 Graduate school, Kyoto Institute of Technology (present address: Yanmar Diesel Engine Co. Ltd., 7-35 Sanwa-cho, Nagahama-city, Shiga pref., 526-0055, Japan).
*3 Graduate school, Kyoto Institute of Technology, Matsugasaki, Sakyo-ku, Kyoto 606-8585, Japan.

Received 25 Decmber 1999.
Revised 13 April 2000.

***Abstract*:** Three-dimensional particle tracking velocimetry (3-D PTV) measurements with a two-camera system have been conducted for a turbulent water plane Couette flow with an oil droplet in order to understand the modification of shear-dominant turbulence by the droplet. The parameters of the stereogrammetry, which are crucial for calculating the spatial coordinate of tracer particles from 2-D images of two cameras, have been determined with a careful calibration. The experimental results show that the axial and wall-normal turbulence intensities and the turbulent kinetic energy are enhanced locally in the confluence regions where axial main flow over the interface meets the secondary flow along the interface in the wall-normal direction. The secondary flows were observed only around the equator of the droplet. The wall-normal and transverse turbulence intensities are found to increase in the region above the droplet. This is due to the change in the direction of the primary flow over the top of the droplet. The turbulence in the other region is attenuated mainly because of the attenuation of the generation and evolution of the coherent structure in the neighbourhood of the droplet.

***Keywords*:** three-dimensional particle tracking velocimetry, two-camera system, turbulent plane Couette flow, immiscible droplet, turbulence modification.

1. Introduction

Interest has been rising recently in the modification of turbulence in liquid flow by immiscible droplets or bubbles dispersed in water flows. Some experimental results showed changes in the turbulence quantities of water flow due to the dispersed phase, such as small particles or small bubbles. However, the interactions between large droplets and large-scale turbulence structure near the droplets are not yet understood. This interaction is crucial for understanding drag reduction in oil flows with water droplets in pipelines (Angeli and Hewitt, 1998), heat transfer in direct-contact heat exchangers, and mass transfer in dissolution processes of liquidised CO_2 into deep sea.

Some pioneering measurements were carried out for the size distribution of immiscible droplets or the overall heat transfer coefficient (Sideman and Taitel, 1964; Lee, 1987). Recently, interaction between an immiscible droplet and its surrounding flow has been investigated (Kaviany, 1994). However, few studies have been done for the modification of near-interface turbulence structure by the immiscible droplets. This is mainly because the droplet dimension is much larger than the smallest scale of the turbulence. The present authors indicated that the droplet deformation and velocity fluctuation induced by the droplet depend on whether the local turbulence including one droplet is classified as an eddy-dominant-, a shear-dominant- or a convergence-dominant-

one (Hagiwara et al., 1997).

We have focused on a turbulent plane Couette flow with an immiscible droplet to understand the modification of shear-dominant turbulence due to the droplet. This flow can be considered to simulate some parts of the actual turbulent shear flows with droplets. The turbulent Couette flows have the following advantages; (i) the linear shear in the core region: (ii) nearly uniform distributions of turbulence intensities in this region: (iii) zero bulk mean velocity. The first two points are useful for examining the turbulence modification due to the droplet. The last point is effective for minimising the influence of fixing the droplet at the centre of the flow on the turbulence structure.

We conducted experiments for a turbulent plane Couette flow with an oil droplet between two moving vertical walls in a horizontal water tank, and carried out a 2-D PTV measurement on the horizontal plane including the centre of the droplet in the case of low Reynolds number (Hagiwara et al., 1998). In this paper, the experimental results of the mean and r.m.s. values of the streamwise fluctuating velocity in the core region showed in agreement with those measured for similar apparatus and condition by Bech et al. (1995). Although PTV has a lower reliability for the spatial resolution due to a lower number density of particles compared with particle image velocimetry (PIV), it has the advantage that three-dimensional measurements can easily be conducted. Furthermore, the number of particles sticking to the interface for PTV is lower than that for PIV. These particles cause error vectors near the interface.

In this study, we carry out a 3-D PTV measurement for the identical Couette flow. Maas (1996) recommended a three-camera system with the camera projective centres forming an equilateral triangle because the ambiguities become smaller than that for a two-camera system. However, the triangle arrangement is almost impossible for the deep, narrow test section in the present study. The difficulties of developing algorithms and programs for the particle image matching and the interface image matching are reduced by using the two-camera system (Engelmann et al., 1998). Therefore, we adopt a two-camera system for the present 3-D PTV. The validity of the present method is examined in the condition where the fluctuating velocity is comparable or higher than the mean velocity in the central core region, thus the error vectors tend to be generated in the image processing.

2. Experimental Method

2.1 Apparatus

A schematic diagram of the experimental apparatus is shown in Fig. 1. This apparatus is the same as that in our previous study (Hagiwara et al., 1998). Water is stored in a rectangular tank of 1800 mm in length, 240 mm in width and up to 190 mm in depth. The main roller, driven directly by a DC motor, and a sub roller were submerged. A transparent belt of 180 mm in width and 0.1 mm in thickness was driven by the main roller and used for the moving walls. To stabilise the motion of the belt, two transparent plates were arranged in parallel as belt guides. Thus, the plane Couette flow with zero bulk velocity was realised between the counter-moving belt with a constant speed of U_w keeping the distance of $2h = 30$ mm. The Reynolds number based on U_w and h was 1.28×10^3, which is nearly equal to both 1260 for the measurement with LDV and 1300 for the direct numerical simulation (DNS) carried out by Bech et al. (1995). In their paper, they exhibited the developed state of turbulence for these numbers by comparing the results for higher Reynolds number cases. Note that the lowest Reynolds number for which turbulence can be sustained was about 360 in the similar experiment (Tillmark and Alfredsson, 1992).

The test section was given at the centre between the two rollers where a developed turbulence field is maintained by the wall-generated turbulence and the roller-generated turbulence. The origin of coordinates was allocated at the centre of the test section. The X, Y and Z axes were positioned in the axial direction of the apparatus, perpendicular to the moving wall and in the transverse direction of the flow, respectively. The volume for the image processing was $50 \times 30 \times 20$ mm^3. The streamwise dimension is the same as that in our previous study (Hagiwara et al., 1998), and is the minimum for observing the flow induced by the presence of the interface. The dimension in the wall-normal direction is the distance between two moving walls.

2.2 Tracer Particle

Nylon 12 particles of the diameter in the range of 0.1-0.2 mm (Daicel-Hüls Ltd. Z2073: specific weight of 1.02) were used for the tracer particles. This size was determined from the square area 0.065×0.065 mm^2 for each pixel of the CCD camera mentioned below to cover in the image-capturing field. If the radius of the image of the tracer

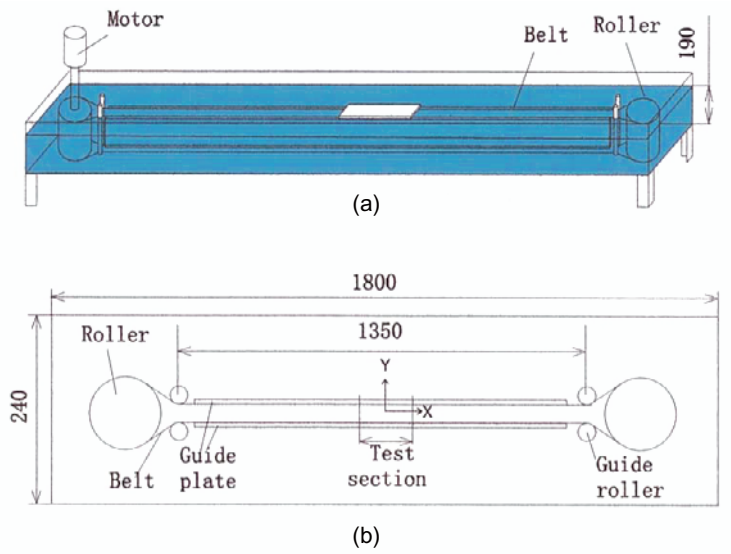

Fig. 1. Experimental apparatus (a) sketch, (b) top view.

particle is shorter than the pixel dimension, the image is covered with at most four pixels, and the gray levels of these pixels are highly dependent on the location of the centre of the particle. Therefore, it is difficult to determine the threshold level for these pixels to identify the particles. To avoid this difficulty, the particle size was determined so that the radii of most of the particles are larger than the pixel size. The upper limit of the frequency beyond which these particles in this size range cease to respond to fluid sinusoidal fluctuation was estimated to be 75 Hz from the result obtaned by Hjelmfelt, Jr. and Mockros (1966).

These characteristics of the tracer particle are compared with those of the small-scale turbulence in the following. The Kolmogorov length scale, l_K, can be expressed by using the DNS result of the dissipation rate of the turbulent kinetic energy, $\varepsilon = 4.1u_\tau^4/\upsilon$, near the axis calculated by Andersson et al. (1992) in the case of $Re = 1300$ as follows:

$$l_K \equiv \left(\frac{\upsilon^3}{\varepsilon}\right)^{1/4} = \frac{\upsilon}{(4.1)^{1/4} u_\tau} = \frac{h}{(4.1)^{1/4} Re_\tau}, \tag{1}$$

where υ is the kinematic viscosity, u_τ is the friction velocity, and Re_τ is the Reynolds number based on the friction velocity. By substituting $Re_\tau = 82.2$ calculated in the paper by Bech et al. (1995) into Eq. (1), l_K is estimated to be 0.13 mm. Therefore, the size of the tracer particle is at most one and a half times larger than l_K.

The highest frequency for the velocity fluctuation is considered to be equal to U/l_K, where U is the local mean velocity. Since the maximum value of U in the central core region ($-0.5 \le Y/h \le 0.5$) is 9.7 mm in the present study, the highest frequency is estimated to be 75 Hz in this region. Thus, the tracer particles can be considered to respond to all the fluctuation in the core region.

2.3 Immiscible Droplet

Silicon oil (Shin-etsu Chemical Inc., KF-99: specific weight of 1.0) was injected into the water from a needle using a syringe to form an immiscible droplet. This droplet was kept at the centre of the test section by a fine rod stood vertically on the bottom plate of the tank throughout the measurement to prevent the droplet from approaching the wall as a result of lift force and velocity fluctuating in the Y direction. The effect of this position-keeping on the deformation and rotation of the droplet is serious in the case of a smaller droplet. Therefore, we focused on the large droplet in the present study, though we can control the droplet size by pulling out the needle from the interface. The diameter of the droplet was 10 mm, which was about 80 times larger than l_K mentioned above.

2.4 Image Capturing

Two progressive-scanning CCD cameras (Sony, XC-8500CE) were set above the tank (See Fig. 2). This camera arrangement is better than any other arrangement because the effects of the moving belt and the guide plate on the images can be minimised. Each camera was mounted on a small turntable. The turntables were fixed on a bed.

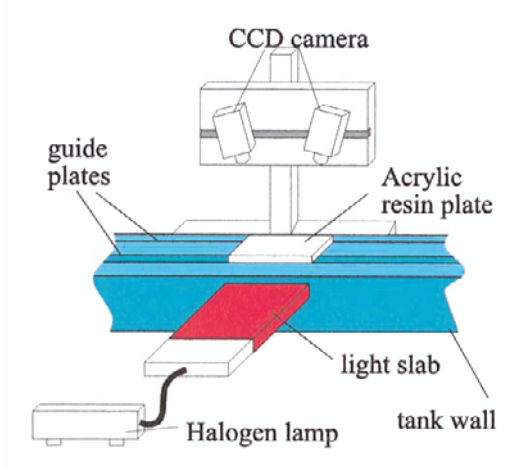

Fig. 2. Camera arrangement and lighting.

The bed was slid on the vertical guide, which was mounted on a horizontal bench. The position of each camera in the X and Z directions was able to be adjusted.

The image capturing of two cameras was synchronised by inputting a trigger signal to the cameras via two frame grabber boards (G-Force Co. Ltd., GF-CP5000). The image-capturing rate was 40 frames per second. The statistical reliability was guaranteed for the fluctuation up to the highest frequency of 20 Hz by the sampling theorem. Most of the flow fluctuation can be captured by the cameras, except small-scale turbulence far from the axis in the core region. However, this small-scale turbulence is found to make little contribution to the statistical quantities, judging from the numerical result for one-dimensional energy spectra (Bech et al., 1995). These spectra show sharp drops at the wave numbers higher than $10/h$, and nearly equal to zero at $60/h$, which corresponds to the frequency lower than 20 Hz. Therefore, the image-capturing frequency is adequate to most of the fluctuation. Each frame consists of 762×572 pixels. A value in the 256-gray-level was assigned to each pixel. The lens aperture and the shutter speed were F1.6 and 1/1000 second, respectively.

The captured images were directly recorded into memories of personal computers without image compression. A total of 500 frames were recorded successively for one series of the image capturing. The images were then stored in hard disks of the computers. Three series of the images were captured.

The light from a halogen lamp was expanded to a light slab of uniform intensity and of 160 mm in length and 20 mm in width by a line light guide made of 320 aligned optical-fibres and a cylindrical lens. The expanded light illuminated the droplet and the particles horizontally from outside the tank through the transparent belt and the transparent belt-guide plate (See Fig. 2).

3. Stereogrammetry

3.1 Method of Orientation of Single Photograph

We adopted the method of orientation of single photograph (Murai et al., 1997) [or the bundle method (Gruen, 1996)] based on the laws of perspective projection. In this method, the object space coordinates of object point, $P(X, Y, Z)$, are evaluated from the measured image coordinates of the point, $p(x, y)$, shown in Fig. 3 by using the following equation:

$$x = -c\frac{a_{11}(X-X_0)+a_{12}(Y-Y_0)+a_{13}(Z-Z_0)}{a_{31}(X-X_0)+a_{32}(Y-Y_0)+a_{33}(Z-Z_0)} + \Delta x$$
$$y = -c\frac{a_{21}(X-X_0)+a_{22}(Y-Y_0)+a_{23}(Z-Z_0)}{a_{31}(X-X_0)+a_{32}(Y-Y_0)+a_{33}(Z-Z_0)} + \Delta y \qquad (2)$$

The components of the rotation matrix between the coordinate system of image and that of object space in Eq. (2)

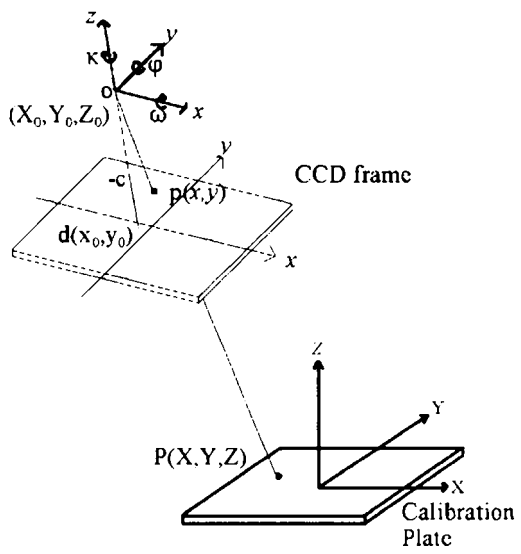

Fig. 3. Coordinates and orientation parameters.

are expressed as follows.

$$a_{11} = \cos\varphi \cos\kappa \qquad a_{12} = -\cos\varphi \sin\kappa \qquad a_{13} = \sin\varphi$$
$$a_{21} = \cos\omega \sin\kappa + \sin\omega \sin\varphi \cos\kappa \qquad a_{22} = \cos\omega \cos\kappa - \sin\omega \sin\varphi \sin\kappa \qquad a_{23} = -\sin\omega \cos\varphi$$
$$a_{31} = \sin\omega \sin\kappa - \cos\omega \sin\varphi \cos\kappa \qquad a_{32} = \sin\omega \cos\kappa + \cos\omega \sin\varphi \sin\kappa \qquad a_{33} = \cos\omega \cos\varphi$$
$$\Delta x = x_0 + \bar{x}\,(k_1 r^2 + k_2 r^4) \qquad \Delta y = y_0 + \bar{y}\,(k_1 r^2 + k_2 r^4)$$
$$r^2 = (\bar{x}^2 + \bar{y}^2)/c^2 \qquad \bar{x} = x - x_0 \qquad \bar{y} = y - y_0.$$

The object space coordinate of the perspective centre, $O(X_0, Y_0, Z_0)$, the rotation angles, $(\omega, \varphi, \kappa)$, the distance between the perspective centre and the CCD frame, c, the correction coefficients for the lens distortion, k_1, k_2 and the image space coordinates of perspective centre, $d(x_0, y_0)$ were evaluated by our iterative procedure mentioned in the next section.

3.2 Orientation Parameters of Camera

Figure 4 shows the iterative procedure for the aforementioned parameters. First, the image space coordinates of reference points were estimated from the original image. The reference points were some grids in the calibration grid, which is made of a thin black plastic plate with white line ruling at a 1 mm square spacing. The plate was on the horizontal bench of the vertical traverse device. The device was placed on the bottom of the tank without water. The discrepancy between the centre of the image space coordinate and $d(x_0, y_0)$ was considered. Secondly, with these image space coordinates, the initial approximation values of the orientation parameters were calculated by solving the second-order equation of perspective projection similar to Eq. (2). Thirdly, the lens distortion was estimated from these initial values. The image space coordinates were corrected by the lens distortion. Then, Eq. (2) was linearised with the Taylor expansion. Next, the correction for the initial approximation values was estimated from the linearised equation. Then, the correction was added to the initial values. Finally, the last two procedures were iterated until the residual error was lower than 5×10^{-6} m on the surface of the CCD chip.

3.3 Particle Image Matching

Figure 5 demonstrates the particle image matching. Since the objective space coordinate of one tracer particle is on the straight line passing through $O(X_0, Y_0, Z_0)$ and $p(x, y)$ for the particle, the intersecting point of two lines for two cameras is the actual location of the tracer particle. If these two straight lines are not intersecting as shown in the circle area of Fig. 5, the midpoint of the line perpendicular to these straight lines was assumed to be the location of the tracer particles. If the minimum distance between two straight lines is larger than 0.3 mm, the location for the tracer particle was not defined. Since the light slab illuminated the particles, the overlapping of two particles on the straight line can occur for one of the 2-D images. This problem was solved by examining the other 2-D image mentioned in Section 4.2.

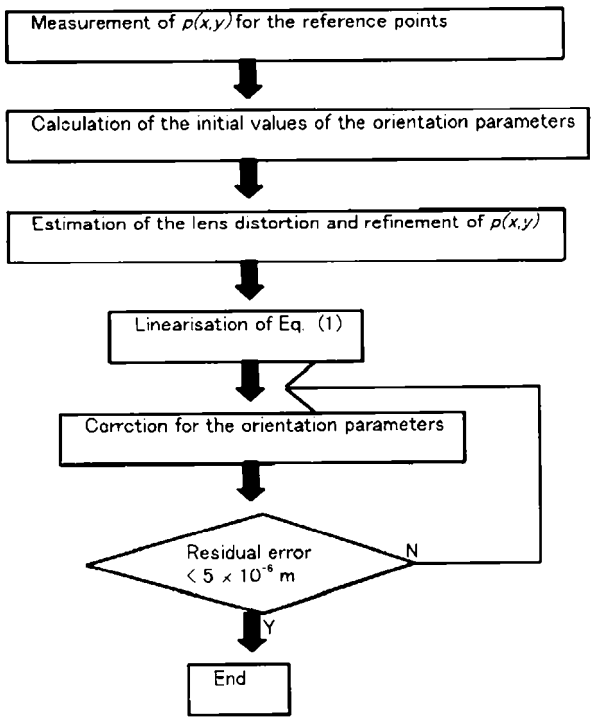

Fig. 4. Procedure for the evaluation of orientation parameters.

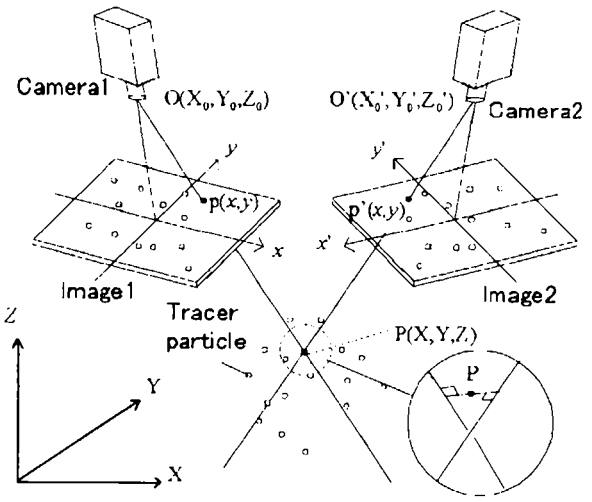

Fig. 5. Particle image matching.

3.4 Compensation of the Light Refraction

To minimise the effect of free surface fluctuation on the images, an acrylic resin plate was put on the belt guide so that the lower half of the plate was submerged and the upper half was in the air. Therefore, the refraction of the light at the upper and lower surfaces of the acrylic plate had to be considered. Based on the method developed by Ninomiya et al. (1995), the exact location of each particle was calculated with Snell's law and the plate thickness after the orientation parameters were evaluated.

4. Image Processing

4.1 Pre-processing of Images

Before the image processing, improvement of the digital images was carried out. First, the nonuniformity of the

shading for the background of the digital images was compensated for by using a reference frame. The reference frame was the median of 17 frames extracted every 0.63 second from the series of captured images. It was confirmed that any particle image was not included in the reference image. Secondly, the neighbourhood averaging technique (Gonzalez and Wintz, 1987) was applied for the smoothing of the images. Finally, binarisation was done to the smoothed images to enhance the particle images. The location of the centre of each particle was thus determined with an error of less than two pixels.

4.2 Particle Velocities

The particle velocity was estimated from the spatial trajectory of the particle. This trajectory was obtained from the particle spatial locations on four successive frames. To decide these locations efficiently, the spatial location for the next time was predicted from the trajectories obtained from the 2-D images. Even if two trajectories of two particles intersect in one 2-D image by the image overlapping of these particles mentioned in Section 3.3, the trajectories and the positions of the particles in space can be identified by analysing the other 2-D image.

4.3 Spatial Interpolation of Velocity Vectors

The velocities of the tracer particles were redistributed to the grid points allocated uniformly in space by a spatial interpolation described as follows:

(i) for a certain grid point, four neighbouring tracer particles were detected,

(ii) if the grid point is inside the triangular pyramid formed by the particles as shown in Fig. 6, the velocity at the grid point, v_g, is estimated by the spatial interpolation of the velocities of the particles as follows:

$$v_g = \frac{mspv_1 + lspv_2 + pt(m+l)v_3 + g(m+l)(s+t)v_4}{(m+l)(s+t)(p+q)} \tag{3}$$

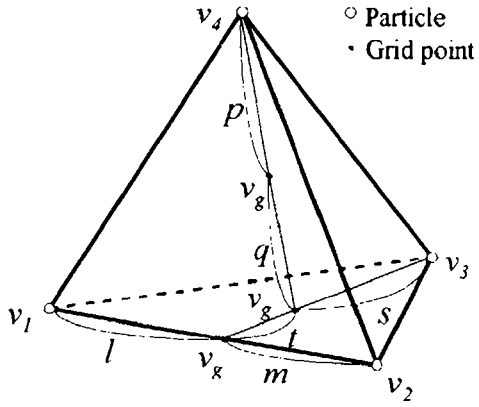

Fig. 6. Velocity interpolation.

(iii) if the grid point is on a surface of the pyramid, the interpolation is done on the surface as follows:

$$v_g = \frac{s(mv_1 + lv_2) + t(m+l)v_3}{(m+l)(s+t)} \tag{4}$$

(iv) if the grid point is on an edge of the pyramid, the interpolation is done along the edge, and v_g is expressed as follows:

$$v_g = \frac{mv_1 + lv_2}{m+l} \tag{5}$$

The present methods of streogrammetry and image processing are basically independent of the specifications of cameras and tracer particles. Therefore, these methods are applicable to the measurement for the other flows.

5. Results and Discussion

5.1 Estimation of Errors

The orientation parameters determined by our iterative procedure were found to be in good agreement with those expected geometrically or those measured. In particular, the difference between the centre of the CCD frame and the image space coordinate of the perspective centre was less than 0.3% of the CCD pixel (Nishino, 1999).

The errors for the objective space coordinate are summarised in Table 1. The errors were estimated by using the plate of calibration grid on the traverse device in the tank with and without water. The plate was positioned at $Z = 20$ and 25 mm ($Z/h = 1.33$ and 1.67) in the case without water and at $Z = 0$ and 5 mm ($Z/h = 0$ and 0.33) in the case with water. A total of 31 grids were selected on the plate for each position. The errors are found to be at most twice as large as the average diameter of the particles. This shows that the present iterative procedure is effective for the determination of the orientation parameters.

Table 1. Errors for the objective space coordinate

	ΔX (mm)	ΔY (mm)	ΔZ (mm)
without water	0.023	0.055	0.174
with water	0.164	0.263	0.297

The error vectors were checked by examining 3-D velocity field reconstructed by the aforementioned procedures at some moments. Figure 7 demonstrates a typical velocity field in the case without the droplet. Note that the box in this figure is wider than that for the image-processing volume in the upper and lower directions. The numbers of the vectors are not so large, because the concentration of the tracer particles is low enough to avoid sticking on the interface, there are some particles which are impossible for the image matching and the tracking through four successive frames. In particular, the particle tracking is not easy for the present case with low mean velocity and high fluctuating velocity. Some error vectors in Fig. 7 are mainly in the regions outside of the image-processing volume or near the moving walls. Therefore, the effect of the error vectors on the statistical quantities is not expected to be serious. The grid points without the vectors were not taken into account for the calculation of mean and r.m.s. values. The accuracy for the statistical quantities examined in the present study is not reduced by this conditional sampling.

The error due to the spatial interpolation described in Section 4.3 was estimated by examining how much mass conservation is satisfied locally. From the mean velocities for the grid points obtained from the interpolation, the divergence for the (i,j,k)-th point is calculated as follows:

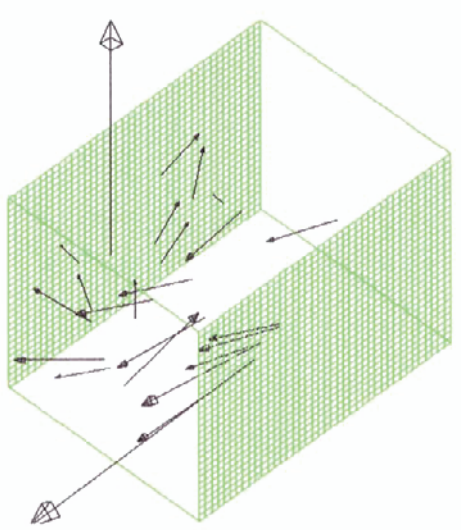

Fig. 7. An example of reconstructed velocity vectors.

$$D_{i,j,k} = \frac{U_{i+1,j,k} - U_{i-1,j,k}}{2\delta} + \frac{V_{i,j+1,k} - V_{i,j-1,k}}{2\delta} + \frac{W_{i,j,k+1} - W_{i,j,k-1}}{2\delta} \tag{6}$$

where δ is the grid spacing. If the mass conservation is satisfied, $D_{i,j,k}$ must be equal to zero. The values of the divergence were scanned for the grid points in the central part in the horizontal plane at $Z = 0$ for the case without the droplet. The absolute value of $D_{i,j,k}$ is found to be smaller than $0.001U_w/h$ for more than 85% of all the points. The worst value of $D_{i,j,k}$ was $0.006U_w/h$ at the corner of the scanned area (i.e., far from the centre of the measuring domain). It is concluded from this result that the mass conservation is satisfied with high accuracy for the mean velocity field obtained by the present spatial interpolation.

5.2 Mean Velocity Distribution without Droplet

Figure 8 indicates the profiles of mean velocities in space and time. The profile of the axial mean velocity was in good agreement with the experimental result for Re = 1262 by Bech et al. (1995) except outside the core region where the reflected light at the moving belt caused error vectors. The wall-normal and transverse mean velocities were nearly equal to zero and less than $0.03U_w$ in the core region.

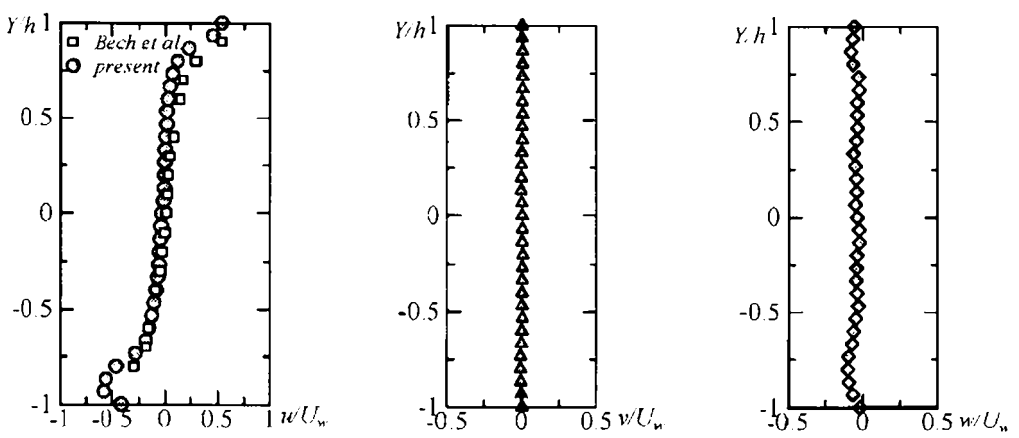

Fig. 8. Mean velocity profiles without droplet.

5.3 Turbulence Intensities without Droplet

Figure 9 shows the profiles of the turbulence intensities without the droplet normalised by u_τ. The friction velocity and the reference data in Fig. 9 were based on the results of Bech et al. (1995). The intensities in the wall-normal and transverse directions, v^* and w^*, in the central core region are in good agreement with the numerical results.

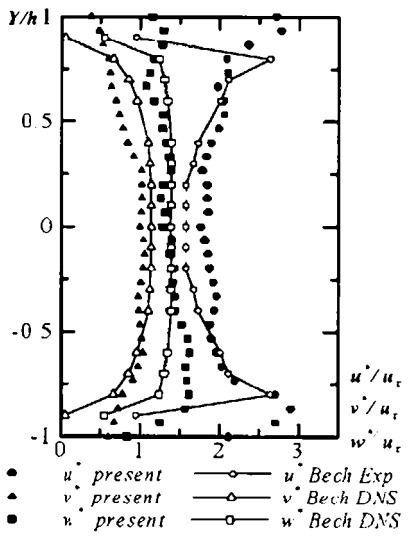

Fig. 9. Turbulence intensities without droplet.

Though the streamwise intensity, u^*, is found to be about 10% higher compared with the experimental result, they show good qualitative agreement with each other. The validities of the present image-capturing and image-processing methods for the core region of the Couette flow are confirmed by the profiles in Figs. 8 and 9. The average values of the intensities over the core region are the reference values for the intensities in case with the droplet adopted in Section 5.6.

5.4 Rotation and Deformation of Droplet

The rotation of the droplet caused by the mean shear was found from the observation of the motion of the tracer particles attached to the interface. The angular velocity of the droplet was about 1.0 rad/s. The circumferential velocity was thus about 0.5 mm/s. This slow velocity is caused by not only the weak support of the droplet with the rod described in Section 2.3 but also the secondary flow along the interface mentioned in the next section.

The deformation of the droplet due to uniform shear can be estimated from the following equation (Stone, 1994):

$$\frac{L-B}{L+B} = Ca\frac{19\lambda+16}{16\lambda+16}, \quad \lambda = \frac{\mu_d}{\mu_c}, \quad Ca = \frac{\mu_c \gamma d}{2\sigma} \tag{7}$$

where L is the longer radius of the droplet, B is the shorter radius, μ_c and μ_d are the viscosity of water and oil respectively, γ is the shear rate, d is the droplet diameter and σ is the interfacial tension. Ca is the capillary number. The deformation is estimated less than 0.2 percent of the radius. The deformation was observed to be less than 3 percent of the droplet diameter, which was larger than the estimated value. The droplet was drawn as a sphere in the following figures.

5.5 Average Velocity Field with Droplet

Figures 10(a), 10(b) and 10(c) indicate the average velocity vectors in the (X, Y)-plane at $Z = 0$. Secondary flows are seen at the side of the droplet (though the one on the left-hand side is smaller than that on the right-hand side in the figure): The main flow bifurcated into the axial flows over the interface and the wall-normal flow along the interface. These flows and the axial primary flow over the interface near the other moving-wall joined in the upper-right and lower-left regions. These secondary flows and their confluence were also observed in our previous 2-D PTV measurement in the identical plane. It is discovered from the present 3-D PTV that the secondary flows and the confluence do not exist in the (X, Y)-plane of $Z = 0.20$ near the top of the droplet. (See Fig. 10(d). Note that only velocity vectors in the plane are plotted in order to avoid confusion.) This is because the primary flow can turn around over the interface at high-latitude of the droplet. It is concluded therefore that the regions of the secondary flows and the confluence are restricted near the 'equator' of the droplet.

5.6 Turbulence Intensities with Droplet

The colour contours for the turbulence intensities are also drawn in Fig. 10. The reference values of the intensities mentioned in Section 5.3 (i.e., the average values of the intensities over the core region) are set at the median of the colour bar (green). Yellow and red in the maps show higher values of intensities, and blue and dark blue show lower values compared with those for the case without the droplet. u^* and v^* take higher values in the confluence regions where the mixing is enhanced by the confluence. This result is in agreement with our previous work.

The regions for higher values of u^* and v^* are found to be restricted around $Z = 0$ in Fig. 11, which is shown by the colour contour map of turbulence intensities in the (Y, Z)-plane at $X/h = 0.70$ including the confluence region. This also shows that the secondary flow exists only near the interface around $Z = 0$ (the equator of the droplet).

We also found increases of v^* (See Fig. 11(c)) and w^* (See Fig. 11(d)) above the droplet where u^* decreased (figure omitted). This is due to the change in the direction of the primary flow over the top of the droplet.

The intensities in the other part of the central region take lower values than those in the case without the droplet. This is because of expected modifications in the coherent structure and its dynamics in the neighbourhood of the droplet: generation of streamwise vortices near the moving walls was attenuated by the droplet, then the evolution of the vortices to horseshoe vortices was also attenuated, and thus the velocity fluctuations caused by these vortices decreased.

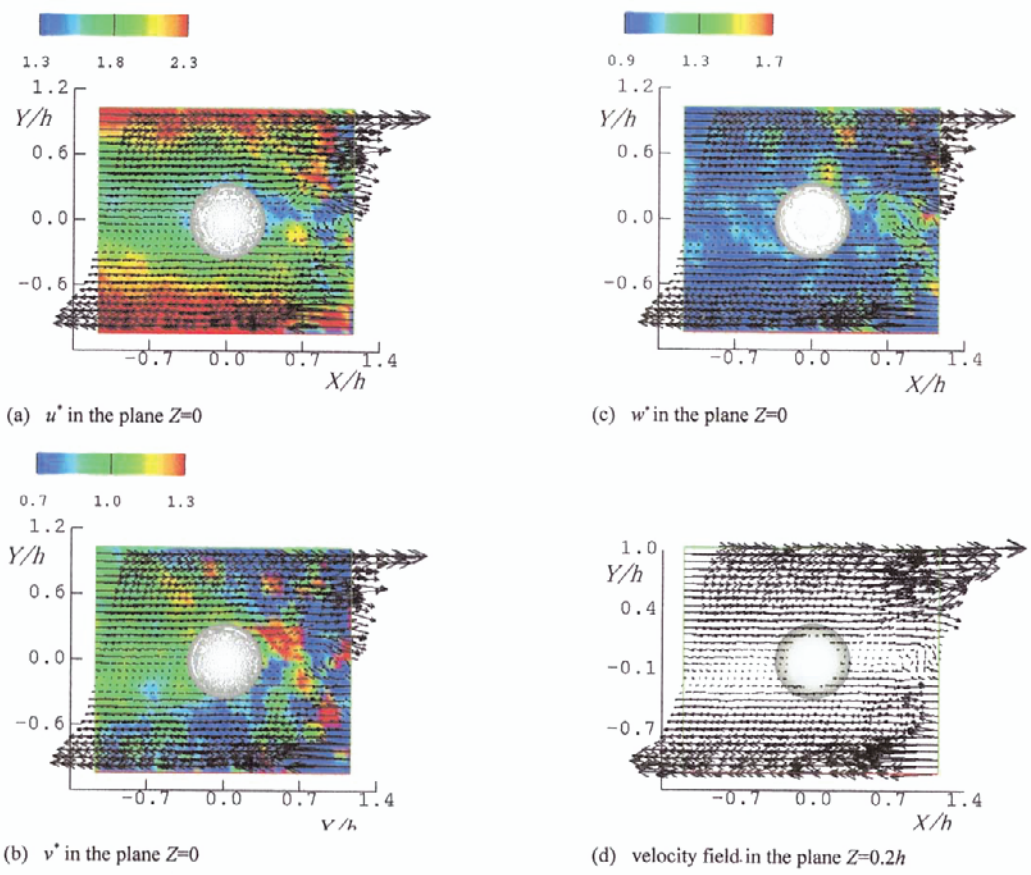

Fig. 10. Mean velocity field and turbulence intensities with droplet in the (*X*, *Y*)-planes.

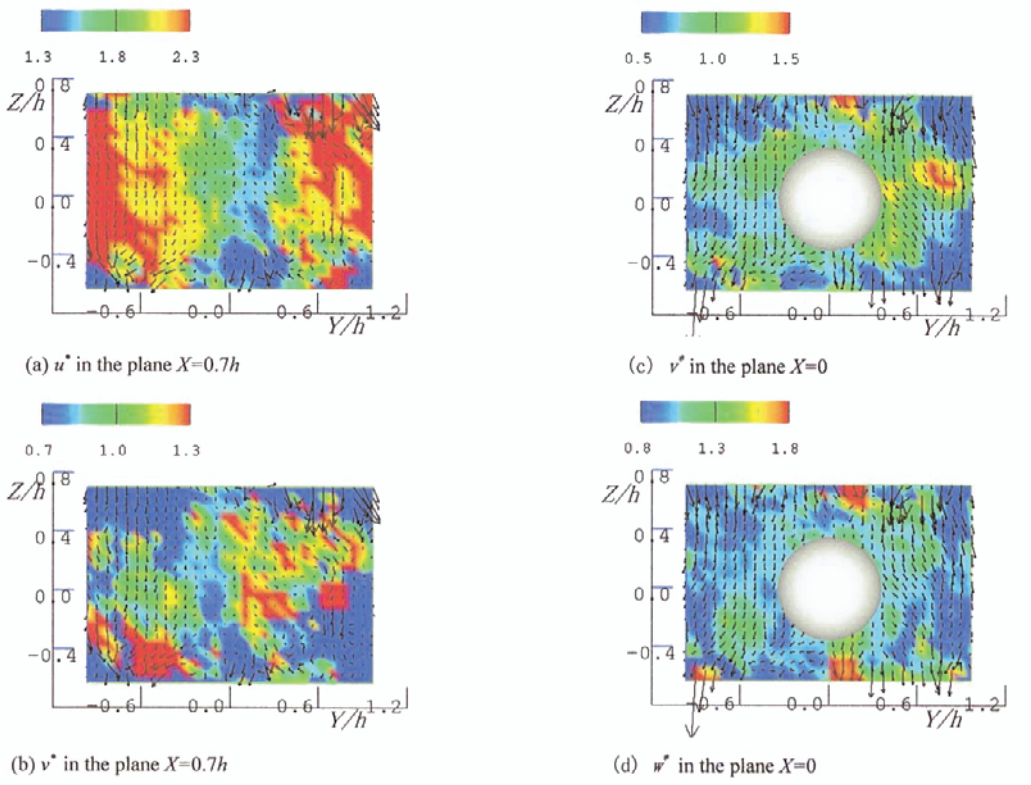

Fig. 11. Turbulence intensities with droplet in the (*Y*, *Z*)-planes.

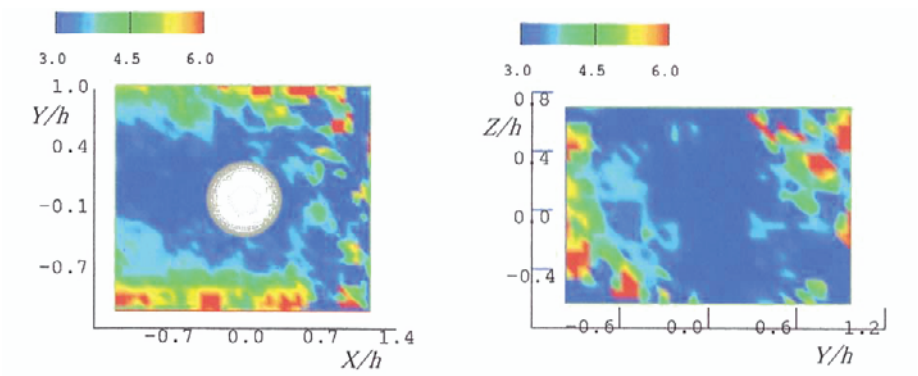

(a) in the (X,Y)-plane (Z=0) (b) in the (Y, Z)-plane (X=0.7h)

Fig. 12. Turbulent kinetic energy with droplet.

5.7 Turbulent Kinetic Energy

Figure 12 shows the distributions of the turbulent kinetic energy, k (= 1/2[u^{*2}+ v^{*2}+ w^{*2}]), with colour contours in the (X, Y)-plane at Z = 0 and the (Y, Z)-plane at X/h = 0.70. The average value of k over the core region in the case without the droplet is drawn green. The areas of dark blue and blue indicate lower values of k, while the areas of yellow and red show higher values. k is found to be attenuated except in the aforementioned confluence regions. This result is in agreement with our previous work. The attenuation of k is due to the modifications in the coherent structure and its dynamics mentioned above. The local enhancement of k is caused by the additional mixing due to the confluence.

6. Conclusion

The experiments were carried out for the turbulent water Couette flow with the oil droplet using the 3-D PTV in the case of low Reynolds number. The droplet was large in order to reduce the effect of the droplet-keeping device on the flow field. The main conclusions obtained are as follows:

(1) The 3-D PTV with two-CCD-camera system, the image-capturing and the image-processing methods developed in the present study are effective for the examination of the modification of near-droplet turbulence. Since these methods are independent of the specifications of cameras and tracer particles, they are applicable to the measurement for the other flows.

(2) The regions of the secondary flows along the interface in the wall-normal direction and the confluence regions of the secondary flow and the primary flow are restricted near the 'equator' of the droplet.

(3) The axial turbulence intensity and the wall-normal turbulence intensity take higher values in the confluence regions due to the mixing by confluence. The wall-normal turbulence intensity and the transverse turbulence intensities increase in the region above the droplet. This is due to the mixing by the change in direction of the primary flow over the top of the droplet.

(4) The turbulent kinetic energy is attenuated by the droplet except in the confluence regions. This is because of the modification in the coherent structure and its dynamics: generation of streamwise vortices near the moving walls was attenuated by the droplet, then the evolution of the vortices to horseshoe vortices was also attenuated, and thus the velocity fluctuations caused by these vortices decreased.

References

Andersson, H. I., Bech, K. H. and Kristoffersen, R., On Diffusion of Turbulent Energy in Plane Couette Flow, Proc. R. Soc. Lond., A 438 (1992), 477-484.

Angeli, P. and Hewitt, G. F., Pressure Gradient in Horizontal Liquid-liquid Flows, Int. J. Multiphase Flow, 24 (1998), 1183-1203.

Bech, K. H., Tillmark, N., Alfredsson, P. H. and Andersson, H. I., An Investigation of Turbulent Plane Couette Flow at Low Reynolds Numbers, Journal of Fluid Mechanics, 286 (1995), 291-325.

Engelmann, D., Garbe, C., Stöhr, M. Geißler, P., Hering, F. and Jähne, B., Stereo Particle Tracking, Proc. of 8th Int. Symp. on Flow Visualization (CD-ROM), (1998), 240.1-240.10.

Gonzalez, R. C. and Wintz, P., Digital Image Processing (Second edition), (1987), 161-175, Addison-Wesley, Reading.

Gruen, A., Videogrammetry: methodology and PTV/LIF applications. In: Three-dimensional Velocity and Vorticity Measuring and Image

Analysis Techniques (ed. by Th. Dracos), (1996), 161-190, Kluwer Academic Pub., Dordrecht.
Hagiwara, Y., None, T., Tanaka, M. and Nishino, M., Turbulence Modification and Interface Deformation in Turbulent Liquid Plane Couette Flow with an Immiscible Droplet, JSME (Japan Soc. Mech. Eng.) Int. J., Series B, 41-2 (1998), 486-492.
Hagiwara, Y., Takashina, Y. and Tanaka, M., Direct Numerical Simulation of the Basic Phase-interactions in Liquid Turbulent Channel Flow with an Immiscible Droplets, Int. J. Nuclear Engineering and Design, 175 (1997), 49-57.
Hjelmfelt, Jr., A. T. and Mockros, L. F., Motion of Discrete Particles in a Turbulent Fluid, Appl. Sci. Res., 16 (1966), 149-161.
Kaviany, M., Principles of Convective Heat Transfer, (1994), 417-425, Springer-Verlag, New York.
Lee, J. M., Drop Size Formations in Agitating Systems. In: Encyclopedia of Fluid Mehcanics (ed. by N. P. Cheremisinoff), (1987), Vol. 6 Chapter 5, 141-165, Gulf Pub. Co., Houston.
Maas, H-G., Contributions of Digital Photogrammetry to 3-D PTV. In: Three-dimensional Velocity and Vorticity Measuring and Image Analysis Techniques (ed. by Th. Dracos), (1996), 191-207, Kluwer Academic Pub., Dordrecht.
Murai, T. et al., Analytical Photogrammetry (in Japanese) (Revised edition), (1997), 10-74, Japan Society of Photogrammetry, Tokyo.
Ninomiya, N., Akiyama, M. and Sugiyama, H., 3-D PTV Velocity Measurement Applied to the Flow in a Complex Flow Geometry (in Japanese), Journal of Visualization Society of Japan, 15 (1995), 279-284.
Nishino, M., Studies on a Turbulent Liquid Couette Flow with an Immiscible Droplet Using PTV (in Japanese). M. Sc Thesis, Kyoto Institute of Technology, 1999.
Sideman, S. and Taitel, Y., Direct-contact Heat Transfer with Change of Phase: Evaporation of Drops in an Immiscible Liquid Medium, Int. J. Heat and Mass Transfer, 7 (1964), 1273-1289.
Stone, H. A., Dynamics of Drop Deformation and Breakup in Viscous Fluids, Annual Review of Fluid Mechanics, 26 (1994), 65-102, Annual Review Inc., Palo Alto.
Tillmark, N. and Alfredsson, P. H., Experiments on Transition in Plane Couette Flow, Journal of Fluid Mechanics, 235 (1992), 89-102.

Author Profile

Yoshimichi Hagiwara: He received his B.Sc. (Eng) degree in mechanical engineering from Kyoto University in 1976, and his Dr. of Eng. in mechanical engineering from Kyoto University in 1982. He had worked for Kyoto University as an instructor and then an associate professor from 1981 to 1994. His research interests were annular and dispersed gas-liquid two-phase flows and heat transfer enhancement. He has worked for Kyoto Institute of Technology as a professor of the control of transport phenomena since 1994. His current research interests are transport phenomena of turbulent liquid-liquid dispersed multiphase flows, drag reduction and attenuation of thermal leakage in turbulent duct flows by adding polymers, and molecular-dynamics simulation of interfacial phenomena.

Masato Nishino: He received his B.Sc. (Eng) degree in mechanical engineering from Kyoto Institute of Technology in 1997 and his M.Sc. degree in mechanical engineering from Kyoto Institute of Technology in 1999. The present paper is mainly based on his Master thesis, in which he developed the 3-D PTV method and discussed the modification of turbulence in the water Couette flow due to the immiscible oil droplet. He has worked for Yanmar Diesel Engine Co., Ltd. since he finished Master Course.

Mitsuru Tanaka: He received his B.Sc. degree in physics from Kyoto University in 1990, and his Dr. of Sci. in Physics from Kyoto University in 1995. He has worked for Kyoto Institute of Technology as a Research Associate in mechanical engineering since then. His current research interests are the simulation on the diffusion of small heavy particles in turbulent flow, the structure and dynamics of homogeneous shear turbulence, and the turbulent Couette flow with immiscible droplets.

Shuji Sakamoto: He received his B.Sc. (Eng) degree in mechanical engineering from Kyoto Institute of Technology in 1999, and is a graduate student in Master Course of Graduate school in Kyoto Institute of Technology. For his Bachelor's thesis, he studied the 3-D PTV method and the modification of turbulence in the water Couette flow due to the immiscible oil droplets by the collaboration with Mr. Nishino. He has been carrying out further refinement of the method during his Master course.